ORIGINAL ARTICLE

CrossMark

Shear stress and blood trauma under constant and pulse-modulated speed CF-VAD operations: CFD analysis of the HVAD

Zengsheng Chen[1] · Sofen K. Jena[2] · Guruprasad A. Giridharan[2,3] · Michael A. Sobieski[2] · Steven C. Koenig[2,3] · Mark S. Slaughter[2] · Bartley P. Griffith[1] · Zhongjun J. Wu[1,4]

Abstract

Modulation of pump speed has been proposed and implemented clinically to improve vascular pulsatility in continuous flow ventricular assist device patient. The flow dynamics of the HVAD with a promising asynchronous pump speed modulation and its potential risk for device-induced blood trauma was investigated numerically. The boundary conditions at the pump inlet and outlet were defined using the pressure waveforms adapted from the experimentally recorded ventricular and arterial pressure waveforms in a large animal ischemic heart failure (IHF) model supported by the HVAD operated at constant and modulated pump speeds. Shear stress fields and hemolysis indices were derived from the simulated flow fields. The overall features of the computationally generated flow waveforms at simulated constant and pulse-modulated speed operations matched with those of the experimentally recorded flow waveforms. The simulations showed that the shear stress field and hemolysis index vary throughout the cardiac cycle under the constant speed operation, and also as a function of modulation profile under modulated speed operation. The computational model did not demonstrate any differences in the time average hemolysis index between constant and modulated pump speed operations, thereby predicting pulse-modulated speed operation may help to restore vascular pulsatility without any further increased risk of blood trauma.

Keywords Continuous flow ventricular assist devices · Speed pulse modulation · Pulsatility · Shear stress · Blood trauma

1 Introduction

Mechanical circulatory support (MCS) with ventricular assist devices (VADs) has become a standard therapy for patients with advanced heart failure (HF) [1, 2]. The first clinically approved pulsatile flow (PF) VADs are large volume displacement pumps that generate pulsatile pressures and flows, but limited by their large size and long-term durability. The continuous flow (CF) VADs based on rotary blood pumps have many technological advantages and have demonstrated better long-term outcomes and reliability than PF-VADs [3]. CF-VADs restore cardiac output while routinely operating at constant pump speeds, but at the expense of diminished pulsatility. Despite significant improvements in rotary pump device design and outcomes, the risks of adverse events associated with MCS devices, such as thromboembolism and stroke, have not been completely eliminated [4, 5]. In addition, other complications uniquely associated with CF-VADs have been observed clinically, including gastrointestinal (GI) bleeding [6] and aortic insufficiency (AI) [7]. It has also been reported that patients with PF-VADs had nearly a threefold increase in the potential for myocardial recovery than patients supported with CF-VADs [8], leading to speculation that vascular pulsatility and phasic volume unloading may play important role(s) in HF reverse remodeling.

To address these limitations, modulation of pump speed with CF-VADs has been proposed as a potential operation strategy to restore vascular pulsatility and help reduce the risk of adverse

✉ Zhongjun J. Wu
zwu@som.umaryland.edu

1   Artificial Organs Laboratory, Department of Surgery, University of Maryland School of Medicine, 10 South Pine Street, MSTF 434A, Baltimore, MD 21201, USA

2   Department of Cardiovascular and Thoracic Surgery, University of Louisville School of Medicine, Louisville, KY 40202, USA

3   Department of Bioengineering, Speed School of Engineering, University of Louisville, Louisville, KY 40292, USA

4   Fischell Department of Bioengineering, A. James Clark School of Engineering, University of Maryland, College Park, MD 20742, USA

events. Bourque et al. implemented an algorithm to alternate the speed of the rotor of a magnetically levitated blood pump between 1500 and 5500 rpm with a modulation rate of 60 bpm and a systolic interval of 30% [9], which became the basis for the HeartMate III (St. Jude Medical, Inc., Pleasanton, CA) artificial pulsatility algorithm in clinical use today. Frazier et al. [10] proposed decreasing the pump flow rate as a potential means to increase vascular pulsatility with the HeartMate II as a means to reduce the risk of GI bleeding and allowing the aortic valve (AV) to periodically open to reduce the risk of AI. Ising et al. [11] investigated a number of candidate flow modulation algorithms to enhance the pulsatility of CF-VADs using computer simulation and mock flow models that demonstrated the ability to generate aortic pulse pressures up to 59 mmHg, reduce left ventricular external work by up to 75%, and improve myocardial perfusion by up to 44% from baseline HF condition. Soucy et al. [12] then investigated the three most promising pump speed modulation algorithms (copulsation, counterpulsation, and low frequency asynchronization) with the HVAD (HeartWare, Miami Lakes, FL) in a chronic ischemic heart failure bovine model demonstrating that synchronous copulsation produced the largest reduction in ventricular volume, counterpulsation produced the largest decrease in ventricular workload and increase in myocardial perfusion, and asynchronous pulsation induced the largest pulsatility (low frequency) with the added benefit of not requiring a physiologic measure (trigger source) for timing device function. Moazami [13] reported that centrifugal pumps are more favorable than axial-flow devices for generating vascular pulsatility with fewer suction events. Nammakie et al. [14] used computational fluid dynamics (CFD) simulation to investigate the possibility of generating pulsatile blood flow via a CF-VAD by adjusting the rotational speed of the pump with two pulsatile patterns (sinusoidal and trapezoidal). They found that the pump speed modulation with a sinusoidal pattern exhibited the potential to achieve an adequate pulsatile flow by precisely controlling the rotational speed compared to that with a trapezoidal pattern. Collectively, these studies successfully

demonstrated the ability to generate vascular pulsatility by modulating CF-VAD pump speed, which resulted in improved hemodynamic efficacy. However, blood flow dynamics and its potential impact on blood trauma have not been thoroughly examined. The particular concern is that the speed modulation will increase the pump speed above the nominal operating speed. A higher operating speed may elevate the shear stress level and transient flow acceleration and deceleration, resulting in additional energy consumption and blood damage.

In this computational study, CFD simulations were performed to assess the internal fluid dynamics and potential for blood trauma with the HVAD operated at fixed speed and low-frequency asynchronous pulse-modulated speed algorithm based upon the findings and recommendations of Soucy et al. [12]. When pump speed is modulated at a rate independent of native heart rate it is called asynchronous. When it is modulated synchronously with heart contraction and relaxation at a rate equal to native heart rate, it is called synchronous. The shear stress (SS) and hemolysis index (HI) were derived from the CFD model-predicted flow fields and compared for the HVAD operated at fixed rate and asynchronous modulated pump speeds.

2 Methods

2.1 Device geometry

The HVAD is a centrifugal flow blood pump which is designed to operate at pump speeds of 1800–4000 rpm with a four-blade rotor supported by a hybrid bearing system consisting of a hydrodynamic thrust axial bearing and a passive magnetic radial bearing and enclosed within a peripheral volute casing (Fig. 1a). The rotor dimension is 34 mm in diameter, and its axial position depends upon weight balance of the magnetic and hydrodynamic forces. The gaps between the top surface of the rotor and the upper housing and the bottom surface of the rotor and the lower housing are
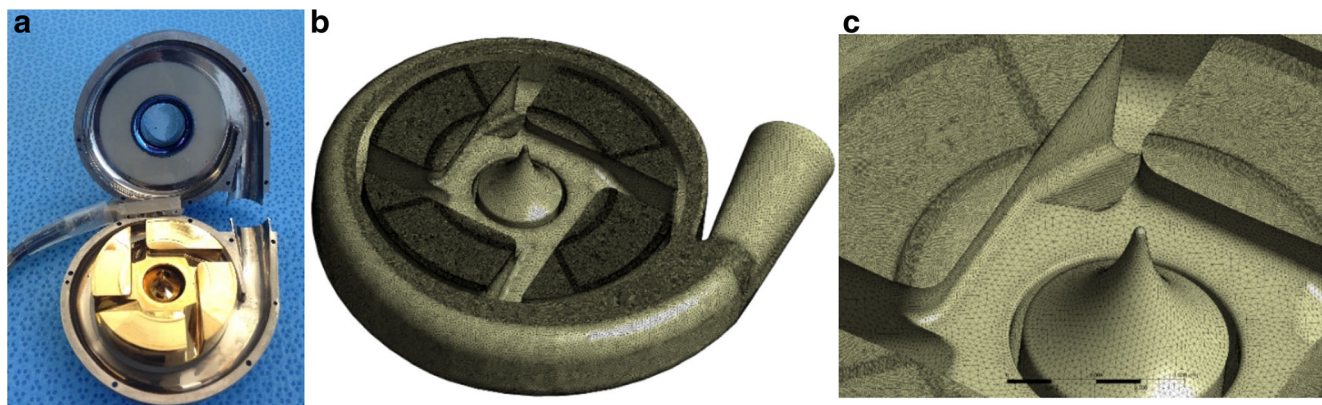
Fig. 1 a Photograph of the disassembled HVAD pump showing the pump housing and impeller. b Unstructured super fined mesh around the impeller. c Enlarged view of unstructured mesh on the impeller surface

40.1 μm and 150.2 μm, respectively. Three-dimensional (3D) precision laser scans of the impeller and housing taken from an explanted clinical HVAD pump were used to obtain the CAD geometry of the pump (CAM Logic, Oxford, MI). The flow domain for analysis was obtained by filling the volume between the rotor and housing with the inlet and outlet tubes using the ANSYS Design modeler (ANSYS, Inc., Canonsburg, PA, USA).

2.2 Meshing

Unstructured meshes of the HVAD pump were generated using the ANSYS Mesh generator. The meshes contain a combination of hexahedral, tetrahedral, and prism elements. The mesh in the rotor blade region and the small gap between the housing and impeller were refined to assure that the sufficiently detailed structure could be resolved (Fig. 1b, c). Inflation layers were included in these regions for more accurate calculation, as these regions are likely to create high SS that contribute to blood trauma. A mesh-independent analysis was completed to assure that the final mesh was valid. For the mesh-independent analysis, we generated three meshes with the same structure but different element sizes, which are the coarse, medium, and fine meshes. The elements for the coarse, medium, and fine meshes are 6.2 million, 8.5 million, and 11.3 million, respectively. The element refinement ratio (r) was calculated by (mesh volume finer/mesh volume coarser)$^{1/3}$. According to the principles outlined by Roache [15], the discretization errors were analyzed. As mesh was refined and the element size decreased, the average discretization error decreased. The mesh with the highest resolution (11.3 million) was selected to perform the CFD simulation.

2.3 Boundary conditions

Pressures at the inlet and outlet of the pump were prescribed as the boundary conditions for the constant and pulse-modulated speed operations. The low frequency asynchronous algorithm (Fig. 2a) and the experimentally recorded aortic and left ventricular pressure waveforms (Fig. 2b) reported by Soucy et al. [12] were used in the CFD simulation for the pulse-modulated speed operation. Similarly, for the constant speed (fixed rate) condition, the rotational speed of the HVAD pump was set at 3000 rpm, and the experimentally recorded pressure and flow waveforms (Fig. 2c) were used [12]. The native left ventricle of the IHF animals retained a degree of contractility as evidenced by the cyclic rise and fall of ventricular pressure during systolic and diastolic phases. During the CFD simulation, we extended the inlet and outlet of the HVAD model to get the fully developed flow, which can create the pressure drop occurs across these extension tubes. Thus, we slightly increase the magnitude of pressure difference across the inlet and outlet by elevating the outlet pressure (aortic pressure) in CFD

model according to the hydrodynamic function curves (HQ curves) of the HVAD pump for producing a targeted flow rate without altering the waveform shape. The pressure and rotor speed waveforms were defined as continuous functions of time through fitted curves of higher order transformation. The mathematical formulae for generating the desired waveforms were written as user defined functions (UDFs), which were compiled and loaded into the fluent library. The walls of the HVAD pump and rotor surface were assumed to be rigid and a no-slip condition was applied to their surfaces.

2.4 Numerical schemes and procedures

The simulations were conducted using the commercial finite volume solver Fluent 15.0 (ANSYS, Inc.). A pressure-based transient solver was chosen with absolute velocity formulation. The blood was assumed to be an incompressible Newtonian fluid with apparent density of 1050 kg/m^3 and viscosity of 0.0035 Pa s [16]. Shear stress transport (SST)-based k-ω model was chosen for turbulence simulation [17] produced as a consequence of high-speed rotation. The rotational motion of the impeller section was defined with the sliding mesh scheme considering the unsteady nature of the flow [18]. SIMPLE (Semi-Implicit Method for Pressure Linked Equations) algorithm with least square cell-based gradient formulation was used for the solution. Residuals of 10^{-3} and 10^{-4} between two successive iterations were chosen respectively for mass continuity and rest primitive variables. All the primitive variables were under-relaxed to obtain the convergence.

2.5 Scalar shear stress and hemolysis calculation

The scalar shear stress (SSS) was derived from the simulated velocity field [19, 20]

$$\sigma = \left[\frac{1}{6}\sum_{i \neq j}\left(\tau_{ii} - \tau_{jj}\right)^2 + \sum_{i \neq j}\tau_{ij}^2\right]^{1/2} \tag{1}$$

where τ_{ij} is the Cartesian components of the SS.

Hemolysis was calculated using the Eulerian scalar transport approach as given in Eq. 2 [20–22]

$$\frac{d\left(hb'\right)}{dt}\rho + v\rho \cdot \nabla\left(hb'\right) = S \tag{2}$$

where v is the velocity vector, S is the source term, ρ is the density of blood, hb' is a transformed scalar variable of released hemoglobin from damaged red blood cells in the flow field, $hb' = hb^{\frac{1}{\alpha}}$, and hb is plasma-free hemoglobin [16]. The source term of Eq. 2 is defined as

Fig. 2 **a** Pulse-modulated speed profile (20 pulses/min). **b** Aortic and ventricular pressure waveforms used for simulation of pulse-modulated speed operation. **c** Aortic and ventricular pressure waveforms used for simulation of constant speed operation. The black dots in **a** and **b** are six discrete time points over two speed pulses which are chosen to compare the hemodynamic performance
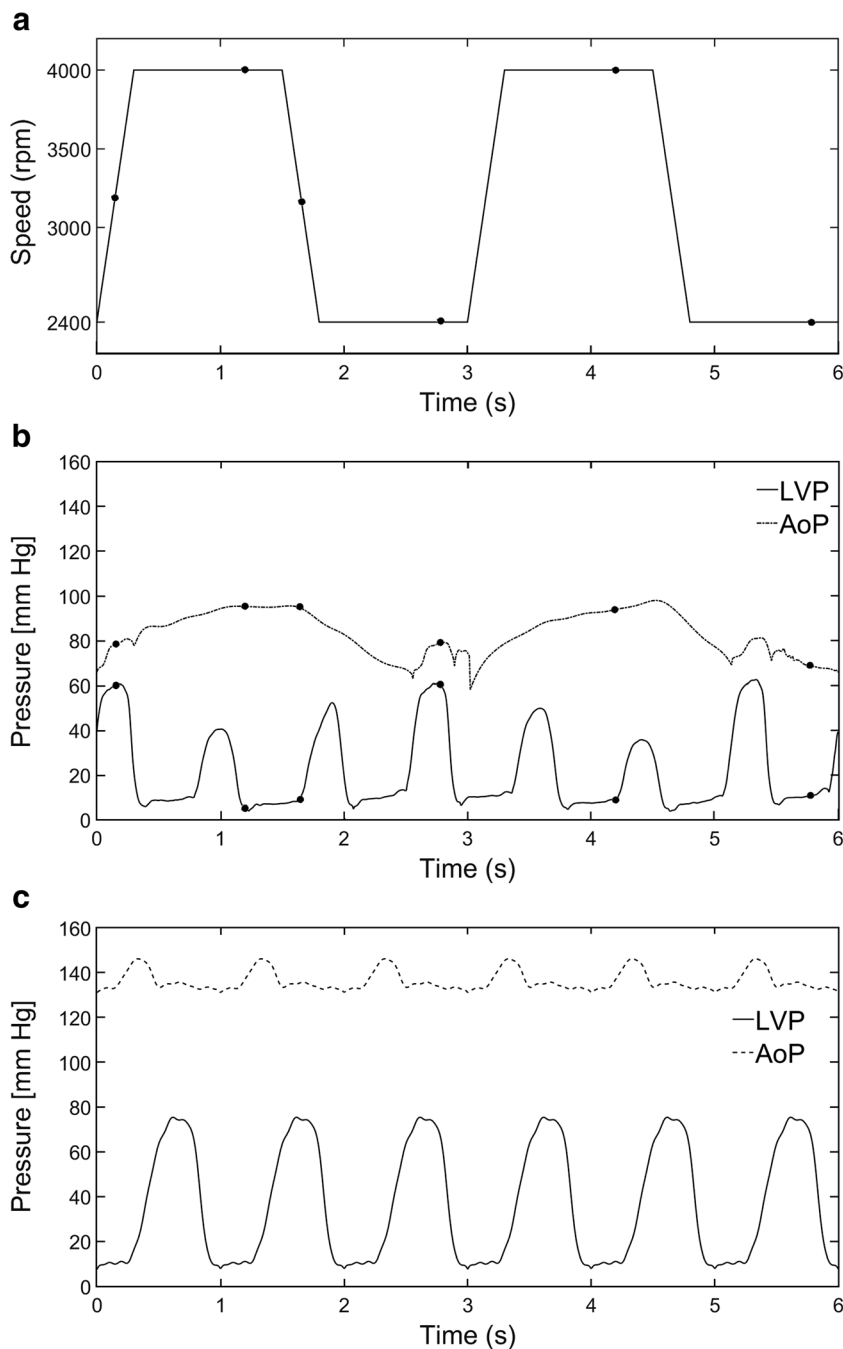
$$S = \rho\left(HB{\cdot}C{\cdot}\sigma^{\beta}\right)^{\frac{1}{\alpha}} \qquad (3)$$

where HB is the total blood hemoglobin concentration, and $HB = 10$ g/dL is used in the present simulation. The empirical coefficients for Eqs. 2 and 3 are $C = 1.8 \times 10^{-6}$, $\alpha = 0.765$, $\beta = 1.991$ [16]. The HI, in percentage, was defined as the ratio of mass-weighted average of hb to HB at the outlet of the pump and expressed as

$$HI(\%) = \frac{\Delta hb}{HB} \times 100 \qquad (4)$$

3 Results

3.1 Device-generated flow waveforms

The CFD-predicted flow waveforms for the pulse-modulated and constant speed operations of the HVAD® pump are shown in Fig. 3a, b, respectively. The landmark features of the resulting flow waveforms were similar to those reported experimentally [12]. The CFD simulation generated an average flow rate of 5.3 L/min during pulse-modulated speed operation, which was slightly higher than recorded

Fig. 3 **a** Computationally predicted flow waveform under pulse-modulated speed operation and **b** computationally predicted flow waveform under constant speed operation. The black dots in **a** are six discrete time points over two speed pulses. The black dots in **b** are six discrete time points over one cardiac cycle
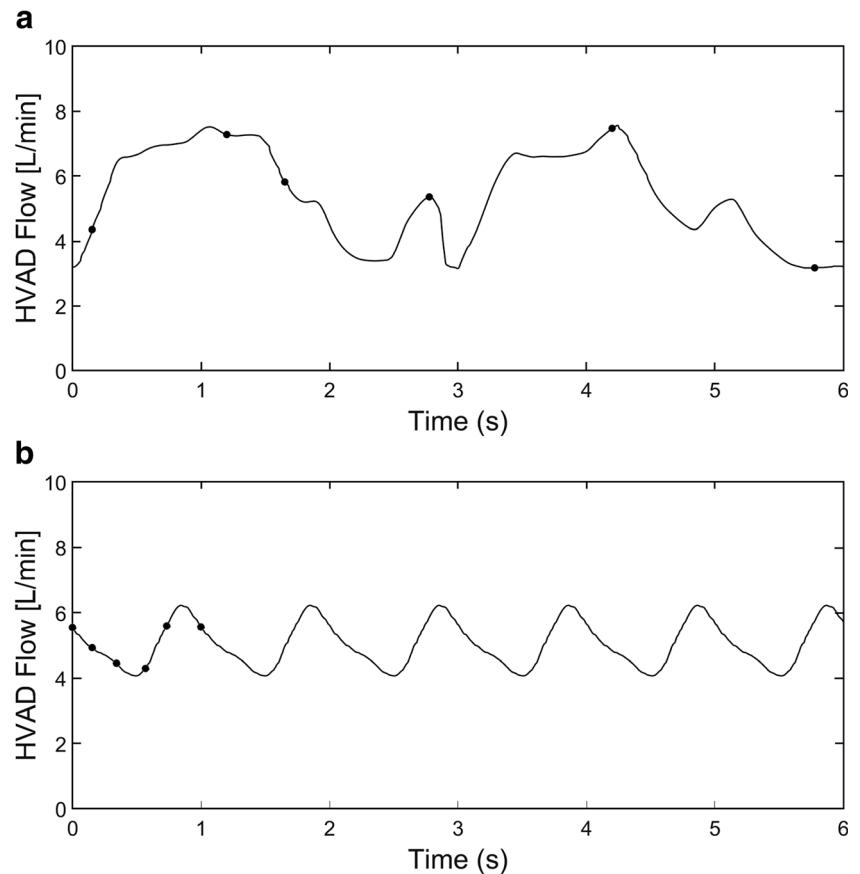
experimentally (4.9 L/min), and 5.0 L/min at constant pump speed (3000 rpm) matching the experimental data [12]. This small difference may have been due to additional pressure loss in the outflow graft (animal data), as well as the flow measurement error, which was not considered in the simulation. The pump flow rate at the constant speed (3000 rpm) varied from 4 to 6 L/min and at pulse-modulated speed operation varied from 3 to 7.5 L/min. As predicted, the modulated pump speed condition produced a greater pulsatility than the constant speed condition. Collectively, these results demonstrated that the CFD model should be valid for the comparison of the flow dynamics, shear stress, and HI during simulated constant and low-frequency, asynchronous modulated pump speeds.

3.2 Shear stress distribution

The wall shear stress (WSS) distribution on the impeller surface of the HVAD pump at six discrete time points for one cardiac cycle during constant speed is shown in Fig. 4. The highest WSS occurred in the narrow hydrodynamic bearing gap between the top wedged surfaces of the impeller and the upper housing. Even with the slight variation in the inlet pressure (left ventricular pressure), the variation of the WSS distribution over the cardiac cycle was negligible. The WSS distribution on the impeller surface at six discrete time points

over two speed pulses under low-frequency asynchronous modulated pump speed operation is shown in Fig. 5. The corresponding times at which the WSS are shown are marked as black dots in the speed, pressure, and flow waveform trace in Figs. 2a, b and 3a. At time $t = 0.15$ s (the middle of the accelerating stage of the rotor), the highest WSS was observed at the hydrodynamic bearing gap between the wedged surfaces of the rotor and the upper housing, and was located in the same region as observed under constant speed operation (Fig. 5). However, the magnitude of the WSS during pulse-modulated speed operation was higher than under constant speed operation. As the rotor speed ramped up to 4000 rpm, the magnitude of the highest WSS increased accordingly and reached a maximum at time $t = 1.2$ s, which corresponds to the time when the pump generated maximum flow. The level of the WSS at the impeller outer edge also approached the highest level. As the impeller speed decreased to 2400 rpm and the pump-generated flow decelerated ($t = 1.65$ s), the WSS decreased. At time $t = 2.78$ s (impeller speed stable at 2400 rpm), the lowest WSS was observed on the impeller surface. Similar WSS findings were observed during the second pulse (Fig. 5).

Volume histograms for SSS of the HVAD pump at six instants under the constant speed and pulse-modulated speed operations are depicted in Figs. 6 and 7, respectively.
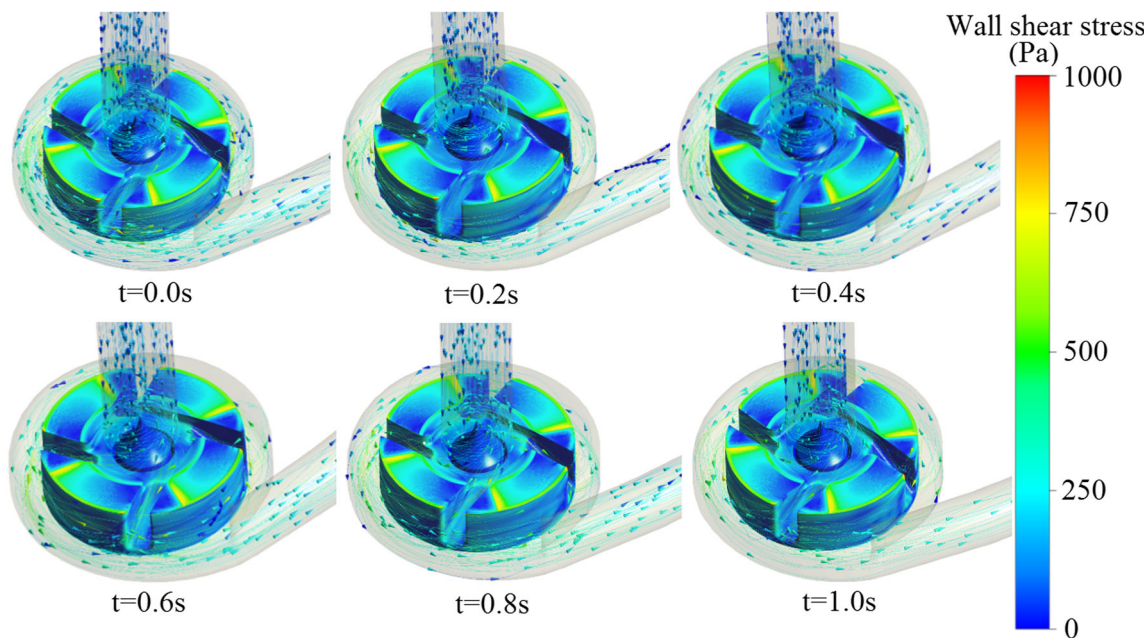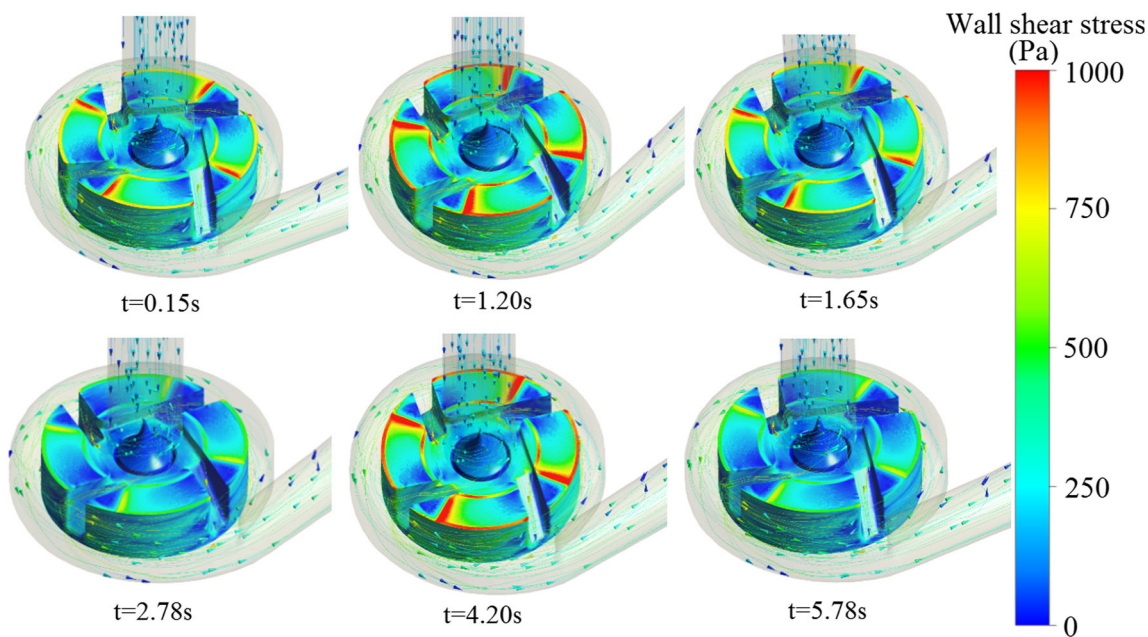
Fig. 4 Simulated wall shear stress distribution on the impeller surface under constant speed operation (3000 rpm) at six discrete time instants over one cardiac cycle

Irrespective of time instant for constant speed operating mode, the maximum scalar stress generated inside the pump reached approximately 1000 Pa at some locations. However, a large volume of the pump was only exposed to lower levels of SSS, and only a very small volume was exposed to SSS above 1000 Pa. These hot spots often existed in the transition region of sharp edges and narrow gaps. During the pulse-modulated speed operation, a higher fraction of the volume was exposed to SS beyond 1000 Pa under the peak rotation speed ($t = 1.2$ s

and 4.2 s in Fig. 7). During the lowest speed rotation, the SSS inside the pumps was below 1000 Pa ($t = 2.78$ s and 5.78 s), and during the mid of acceleration and deceleration stage, it was comparable to the trend of constant speed rotation ($t = 0.15$ s and 1.65 s).

The fluid volumes exposed to SSS were grouped into three categories according to the SSS levels: (1) below 10 Pa, which is within the physiological range, (2) above 10 Pa and below 100 Pa, which is considered to be non-physiological, and (3)

Fig. 5 Simulated wall shear stress distribution on the impeller surface at six discrete time instants over two speed pulses under pulse-modulated speed operation
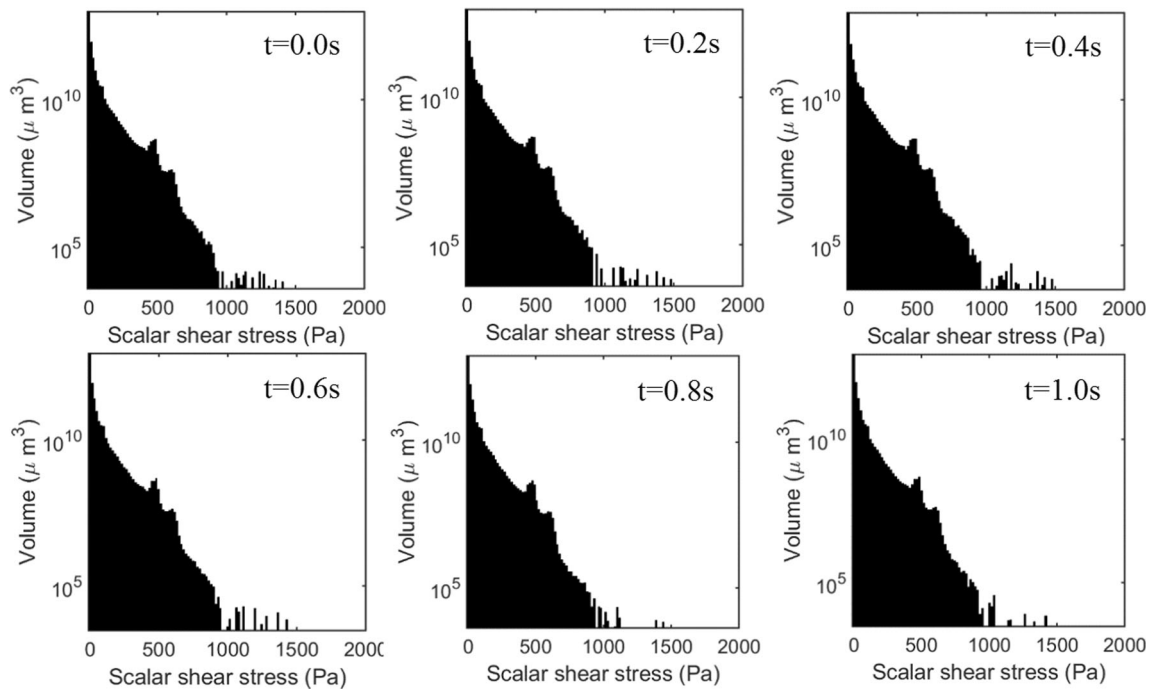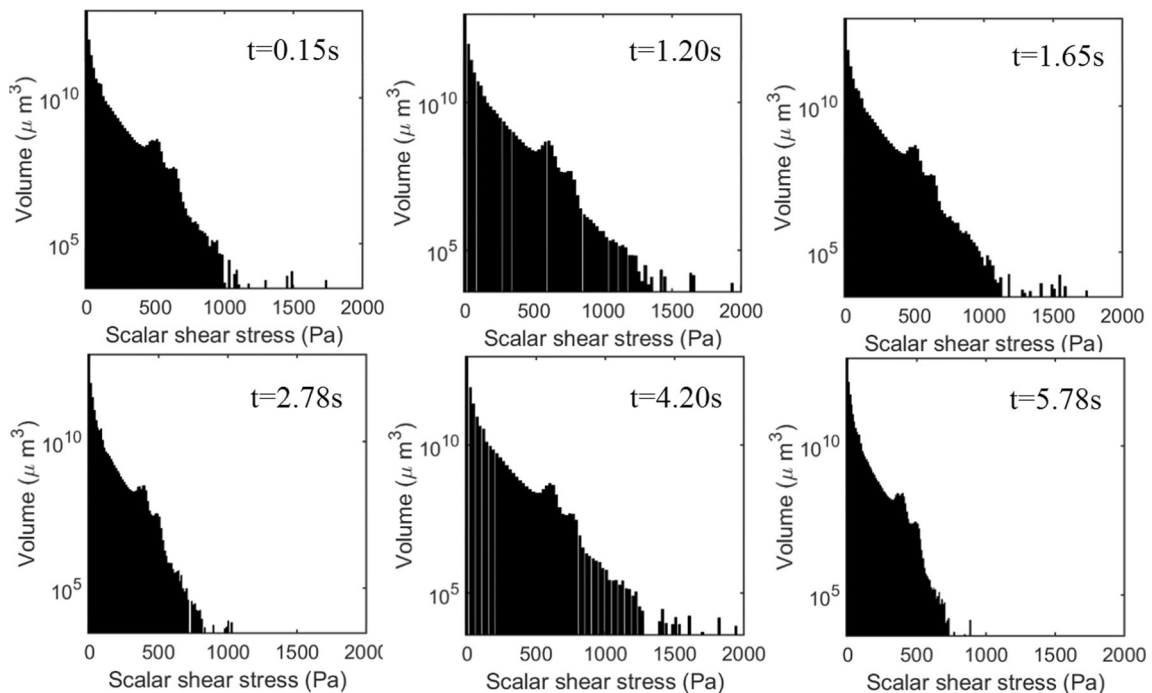
Fig. 6 Histogram of volumetric SSS distribution inside the pump at six discrete time instants under constant speed rotation operation (3000 rpm)

beyond 100 Pa, which is extremely non-physiological. The exposure to non-physiological shear stress may cause platelet activation and hemolysis while the exposure to extremely non-physiological shear stress could induce structural and functional impairment of blood cells, including platelet activation, receptor shedding, and cellular rupture [23, 24]. A summary of the SSS distribution for the three exposure zones is shown in Fig. 8a, b.

Under the constant speed operation, about 75–77% of the volume inside the pump was exposed to SSS below 10 Pa while almost 22–24% of volume was exposed to SSS from 10 to 100 Pa. Only a small fraction of the volume around 0.6 to 0.7% was exposed to SSS above 100 Pa (Fig. 8a).

Under the pulse-modulated speed operation, the percentage of the volumes exposed to the three levels of SSS varied at

Fig. 7 Histogram of volumetric SSS distribution inside the pump at six discrete time instants over two speed pulses under pulse-modulated rotation operation

Fig. 8 Percentages of volumes with physiological SSS, non-physiological SSS, and extreme non-physiological SSS at six discrete time instants, **a** under constant speed (3000 rpm) operation and **b** under pulse-modulated rotation operation
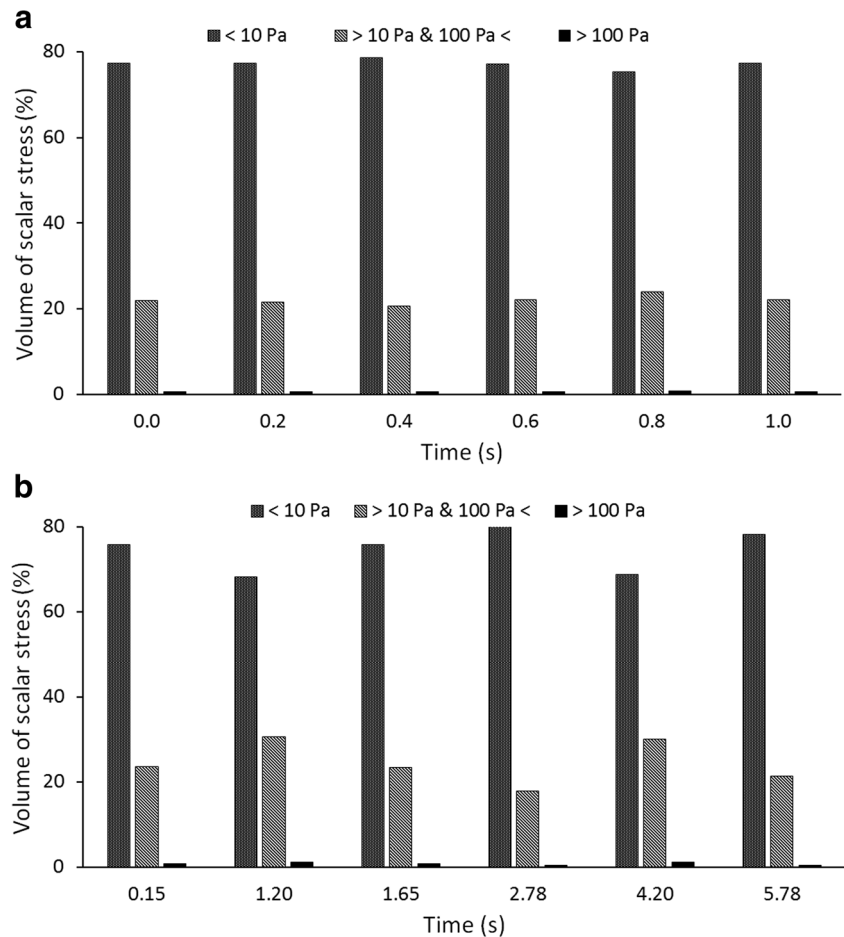
different instants due to variation in pump speed (2400–4000 rpm) (Fig. 8b). At the middle of acceleration and deceleration ($t = 0.15$ s and 1.65 s), about 75% of the volume was exposed to SSS below 10 Pa, 23% of the volume to SSS from 10 to 100 Pa, and about 0.75% of the volume to SSS above 100 Pa. While the pump speed was at 4000 rpm, the volume exposed to higher SSS levels increased. About 68% of the volume was exposed to SSS below 10 Pa and 30% of the volume to SSS from 10 to 100 Pa while about 1% of the volume was exposed to SSS above 100 Pa. During the low-speed rotation at 2400 rpm, around 80% of pump volume are exposed to SSS below 10 Pa, 17–22% of the volume to SSS from 10 to 100 Pa, and a smaller percentage (< 0.5%) of the volume to SSS above 100 Pa.

3.3 Hemolysis analysis

The HI was calculated from the solution of the scalar transport Eq. 2 in an Eularian frame from the flow field variables [15, 19]. In order to quantitatively characterize the device-induced blood trauma under the constant and pulse-modulated speed operations, HI defined in Eq. 4 was used to denote the ratio of plasma-free hemoglobin to the total blood hemoglobin concentration at any

instant of time. The predicted HI results are presented in Fig. 9a, b. As indicated by Fig. 9a, the high HI exists in the gaps between the impeller top surface and the upper housing, and the impeller bottom surface and the lower housing wall, and the impeller inner wall and the central strut. The HI varied with modulated pump speed and cardiac cycle (Fig. 9a, b). The hemolysis was highest at pump speeds of 4000 rpm and lowest at pump speeds of 2400 rpm (Fig. 9a, b). The HI for the constant speed condition also varied periodically with the cardiac cycle with maximum at the lowest flow rate and the minimum at the highest flow rate. The variation range of the HI under the pulse-modulated speed operation was much larger than that under the constant speed condition. Ultimately, the differences in the time-averaged value of the HI for the constant (2.97×10^{-6}) and modulated (2.91×10^{-6}) pump speeds are assumed to be negligible, suggesting no additional risk for hemolytic dysfunction with low-frequency asynchronous pump speed modulation.

4 Discussion

CF-VADs have gained widespread clinical acceptance and use as a viable HF therapy having successfully demonstrating

Fig. 9 Computationally predicted time-varying HI generated by the HVAD pump under the two operation modes: constant speed and pulse-modulated speed. **a** The contour maps of the hemolysis index (HI) distribution on the middle cut plane of the HVAD pump at 0.2 s and 0.4 s under constant speed condition and 1.2 s (speed of 4000 rpm) and 2.78 s (speed of 2400 rpm) under pulse-modulated speed condition. **b** The time-varying HI values; dash line is for constant speed operation and solid line is for pulse-modulated speed operation
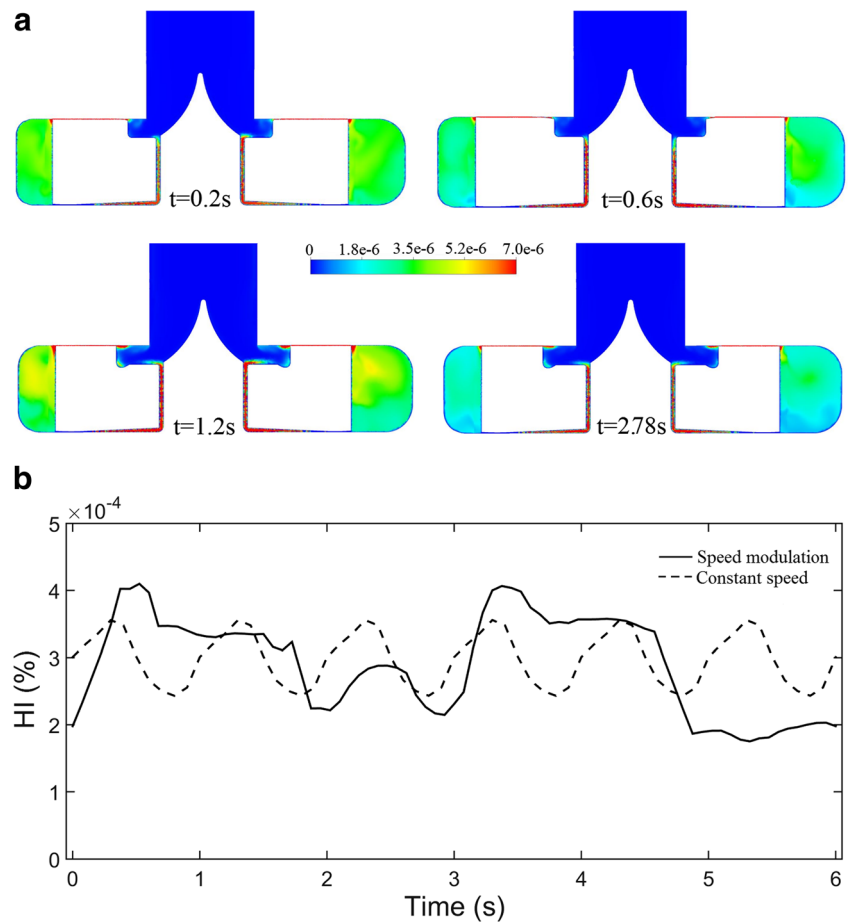
better outcomes than PF-VADs. However, the risk of clinically significant adverse events has not been completely eradicated [25]. The diminished vascular pulsatility, continuous volume unloading, and/or non-physiologic shear stresses produced by CF-LVADs have been hypothesized as potential contributing factors. For example, endothelium and smooth muscle cells sense the arterial pulse and adapt to cyclic changes of pressure and flow to maintain the normal homeostasis. Under the constant speed operation, CF-VADs not only diminish the vascular pulsatility, but may also cause permanent closure of the AV [26]. Ambardekar et al. [27] reported that there were changes in the structure and composition of the aorta as well as an increase in aortic wall stiffness in CF-VAD patients without AV opening compared with age-matched HF patients and non-failing donors.

The potential clinical benefits of vascular pulsatility and conversely the potential consequences of non-physiologic (diminished) pulsatility have been debated for decades. Nonetheless, clinically approved devices have implemented algorithms to alter CF-VAD pump speed to enable opening of the AV and/or washing device bearings to help prevent thrombus [28]. Pulsatility index (PI) is often used in the literature to characterize the physiological pulse and is often defined as the ratio of the difference between maximum (peak)

and minimum (valley) flow rates to the average flow rate. In this CFD study, analysis of the two operation modes of the HVAD pump, the PI for the constant speed operation was 0.43 while the PI for the pulse-modulated speed operation was 0.82. The pulse-modulated speed operation almost doubled the PI. Based on the analyses of the SS distribution and HI, low-freqeuncy asynchronous pump speed modulation doubled the PI while predicting no discernible difference in hemocompatibility compared to constant pump speed.

Analysis of CFD data demonstrated the WSS and SSS vary as a function of cardiac cycle and pump speed. As indicated by the results, it can be found that the shear stress level near the rotor is closely related to pump speed. When the pump speed is fixed, the flow rate changes because of the variation of inlet and outlet presure, and the WSS and SSS around rotor still nearly keep the same. However, when pump speed increases, the WSS and SSS elevate, and vice versa. It has also been shown that shear stress is the primary culprit of blood trauma. In this computational study, HI fluctuated during the constant speed operation due to the ventricular contraction, but the magnitude of the fluctuation was relatively small. As the WSS and SSS changed with the rotor speed under the pulse-modulated speed operation, hemolysis was higher during the high-speed rotation and lower during the low-speed rotation, but the time-averaged values of the HI for

both the constant and pulse-modulated speed operations were comparable. These results support the basis for continued investigation of CF-VAD pump speed modulation to create vascular pulsatility and phasic volume unloading as a potential control strategy to help to mitigate potential complications without further risk of additional blood trauma. The findings of the present study can be used as a reference for the pulse-modulated speed operation of HAVD in clinical trials in coming days.

Some limitations should to be mentioned. (1) The blood was assumed to be Newtonian fluid. The non-Newtonian characteristics were not incorporated in the simulation. (2) The gap of the HVAD was set to be constant for simulation. While during the speed changing of rotor, there might be quite small change of gap size because of the weight balance of the magnetic and hydrodynamic forces whose effect on our simulation can be practically neglected. (3) The pressure waveforms generated from the in vivo calf experiments may differ from clinical waveforms due to differences in vascular impedance between the calf and human heart failure. (4) The present work is only a comparative study using the linearized power law model to calculate HI under pulsatile flow condition. The applicability of this model for pulsatile flow condition needs to be experimentally validated. In additon, it is premature to make a conclusion based solely on a CFD study and experiments will be needed to verify the blood damage under the constant and pulse-modulated speed operations.

5 Conclusion

Low-frequency, asynchronous pump speed modulation with CF-VAD (HVAD) increased vascular pulsatility (doubled PI) compared to constant pump speed. Although pump speed modulation generated larger variations in the stress field and HI, the time-averaged values were indiscernible compared to fixed rate (3000 rpm). These findings suggest that the pulse-modulated speed operation of a CF-VAD may be a feasible technique to restore the vascular pulsatility without further increasing the risk of blood trauma.
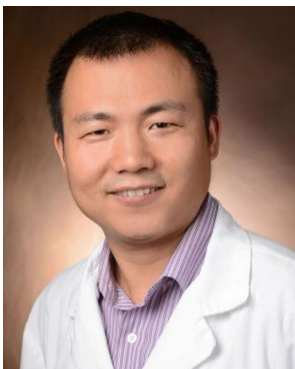
Compliance with ethical standards

Conflict of interest The authors declare that they have no conflicts of interests.

References

1. Mozaffarian D, Benjamin EJ, Go AS, Arnett DK, Blaha MJ, Cushman M, de Ferranti S, Després JP, Fullerton HJ, Howard VJ, Huffman MD, Judd SE, Kissela BM, Lackland DT, Lichtman JH, Lisabeth LD, Liu S, Mackey RH, Matchar DB, McGuire D, Mohler ER III, Moy CS, Muntner P, Mussolino ME, Nasir K, Neumar RW, Nichol G, Palaniappan L, Pandey DK, Reeves MJ, Rodriguez CJ, Sorlie PD, Stein J, Towfighi A, Turan TN, Virani SS, Willey JZ, Woo D, Yeh RW, Turner MB, American Heart Association Statistics Committee and Stroke Statistics Subcommittee (2015) Heart disease and stroke statistics—2015 update: a report from the American Heart Association. Circulation 131(4):e29–e322

2. Slaughter MS, Rogers JG, Milano CA, Russell SD, Conte JV, Feldman D, Sun B, Tatooles AJ, Delgado RM III, Long JW, Wozniak TC, Ghumman W, Farrar DJ, Frazier OH, HeartMate II Investigators (2009) Advanced heart failure treated with continuous-flow left ventricular assist device. N Engl J Med 361(23):2241–2251

3. Loor G, Gonzalez-Stawinski G (2012) Pulsatile vs. continuous flow in ventricular assist device therapy. Best Pract Res Clin Anaesthesiol 26(2):105–115. https://doi.org/10.1016/j.bpa.2012.03.004

4. Sifain AR, Schwarz KQ, Hallinan W, Massey HT, Alexis JD (2014) Ventricular assist device thrombosis following recovery of left ventricular function. ASAIO J 60(2):243–245

5. Morgan JA, Brewer RJ, Nemeh HW, Gerlach B, Lanfear DE, Williams CT, Paone G (2014) Stroke while on long-term left ventricular assist device support: incidence, outcome, and predictors. ASAIO J 60(3):284–289

6. Crow S, John R, Boyle A, Shumway S, Liao K, Colvin-Adams M, Toninato C, Missov E, Pritzker M, Martin C, Garry D, Thomas W, Joyce L (2009) Gastrointestinal bleeding rates in recipients of nonpulsatile and pulsatile left ventricular assist devices. J Thorac Cardiovasc Surg 137:208–215

7. Pak SW, Uriel N, Takayama H, Cappleman S, Song R, Colombo PC, Charles S, Mancini D, Gillam L, Naka Y, Jorde UP (2010) Prevalence of de novo aortic insufficiency during long-term support with left ventricular assist devices. J Heart Lung Transplant 29:1172–1176

8. Krabatsch T, Schweiger M, Dandel M, Stepanenko A, Drews T, Potapov E, Pasic M, Weng YG, Huebler M, Hetzer R (2011) Is bridge to recovery more likely with pulsatile left ventricular assist devices than with nonpulsatile-flow systems? Ann Thorac Surg 91(5):1335–1340

9. Bourque K, Dague C, Farrar D, Harms K, Tamez D, Cohn W, Tuzun E, Poirier V, Frazier OH (2006) In vivo assessment of a rotary left ventricular assist device-induced artificial pulse in the proximal and distal aorta. Artif Organs 30(8):638–642

10. Frazier OH (2010) Unforeseen consequences of therapy with continuous-flow pumps. Circ Heart Fail 3(6):647–649

11. Ising M, Warren S, Sobieski M, Slaughter M, Koenig S, Giridharan G (2011) Flow modulation algorithms for continuous flow left ventricular assist devices to increase vascular pulsatility: a computer simulation study. Cardiovasc Eng Technol 2:90–100

12. Soucy KG, Giridharan GA, Choi Y, Sobieski MA, Monreal G, Cheng A, Schumer E, Slaughter MS, Koenig SC (2015) Rotary pump speed modulation for generating pulsatile flow and phasic left ventricular volume unloading in a bovine model of chronic ischemic heart failure. J Heart Lung Transplant 34(1):122–131

13. Moazami N, Fukamachi K, Kobayashi M, Smedira NG, Hoercher KJ, Massiello A, Lee S, Horvath DJ, Starling RC (2013) Axial and centrifugal continuous-flow rotary pumps: a translation from pump mechanics to clinical practice. J Heart Lung Transplant 32:1–11

14. Nammakie E, Niroomand-Oscuii H, Koochaki M, Ghalichi F (2017) Computational fluid dynamics-based study of possibility of generating pulsatile blood flow via a continuous-flow VAD. Med Biol Eng Comput 55(1):167–178

15. Roache PJ (1997) Quantification of uncertainty in computational fluid dynamics. Annu Rev Fluid Mech 29:123–160

16. Fraser KH, Zhang T, Taskin ME, Griffith BP, Wu ZJ (2012) A quantitative comparison of mechanical blood damage parameters

in rotary ventricular assist devices: shear stress, exposure time and hemolysis index. J Biomech Eng 134(8):081002

17. Menter FR (1994) Two-equation eddy-viscosity turbulence models for engineering applications. AIAA J 32:1598–1605

18. Jung Y, Baek J (2008) A numerical study on the unsteady flow behavior and the performance of an automotive sirocco fan. J Mech Sci Technol 22(10):1889–1895

19. Bludszuweit C (1995) Model for a general mechanical blood damage prediction. Artif Organs 19:583–598

20. Taskin ME, Fraser KH, Zhang T, Wu C, Griffith BP, Wu ZJ (2012) Evaluation of Eulerian and Lagrangian models for hemolysis estimation. ASAIO J 58(4):363–372

21. Farinas MI, Garon A, Lacasse D, N'dri D (2006) Asymptotically consistent numerical approximation of hemolysis. J Biomech Eng 128:688–696

22. Zhang J, Gellman B, Koert A, Dasse KA, Gilbert RJ, Griffith BP, Wu ZJ (2006) Computational and experimental evaluation of the fluid dynamics and hemocompatability of the centrimag blood pump. Artif Organs 30:168–177

23. Zhang T, Taskin ME, Fang HB, Pampori A, Jarvik R, Griffith BP, Wu ZJ (2011) Study of flow-induced hemolysis using novel Couette-type blood-shearing devices. Artif Organs 35(12):1180–1186

24. Chen Z, Mondal NK, Ding J, Koenig SC, Slaughter MS, Wu ZJ (2016) Paradoxical effect of nonphysiological shear stress on platelets and von Willebrand factor. Artif Organs 40(7):659–668

25. Hasin T, Deo S, Maleszewski JJ, Topilsky Y, Edwards BS, Pereira NL, Stulak JM, Joyce L, Daly R, Kushwaha SS, Park SJ (2014) The role of medical management for acute intravascular hemolysis in patients supported on axial flow LVAD. ASAIO J 60(1):9–14

26. Adamson RM, Dembitsky WP, Baradarian S, Chammas J, May-Newman K, Chillcott S, Stahovich M, McCalmont V, Ortiz K, Hoagland P, Jaski B (2011) Aortic valve closure associated with HeartMate left ventricular device support: technical considerations and long-term results. J Heart Lung Transplant 30(5):576–582

27. Ambardekar AV, Hunter KS, Babu AN, Tuder RM, Dodson RB, Lindenfeld J (2015) Changes in aortic wall structure, composition, and stiffness with continuous-flow left ventricular assist devices: a pilot study. Circ Heart Fail 8:944–952

28. Tolpen S, Janmaat J, Reider C, Kallel F, Farrar D, May-Newman K (2015) Programmed speed reduction enables aortic valve opening and increased pulsatility in the LVAD-assisted heart. ASAIO J 61(5):540–547

Sofen K. Jena , Ph.D., received his Ph.D. degree at Jadavpur University (India) in 2014 and is now the Lead CFD Analyst at Faurecia Emissions Control Technologies (Bangalore, India).

Guruprasad A. Giridharan , Ph.D., received his Ph.D. degree in chemical engineering from the University of Utah, Salt Lake City, UT, in 2002. He is now Associate Professor in Department of Bioengineering at the University of Louisville.

Michael Sobieski , RN, CCP., received his nursing degree from Morton College. He is now the Director of Translational Research and Artificial Organs in Department of Cardiovascular and Thoracic Surgery at the University of Louisville.

Zengsheng Chen , Ph.D., received his Ph.D. degree at Beihang University (Beijing, China) in 2011. He is now an Instructor at Surgery Department in University of Maryland School of Medicine.

Steven C. Koenig , Ph.D., received his Ph.D. from University of Texas in 1996 and is currently a Professor of Bioengineering and Cardiovascular and Thoracic Surgery in University of Louisville.

Bartley P. Griffith , M.D., is now the Thomas E. and Alice Marie Hales Distinguished Professor in Transplant Surgery, University of Maryland School of Medicine.

Mark S. Slaughter , M.D., received his M.D. from Indiana University School of Medicine in 1986 and is now the Professor and Chief of Department Cardiovascular and Thoracic Surgery in University of Louisville.

Zhongjun J. Wu , Ph.D., received his Ph.D. from University of Miami in 1996 and is now the Peter Angelos Distinguished Professor in Entrepreneurial Surgical Science Department of Surgery, University of Maryland School of Medicine.